



## OPEN ACCESS

## EDITED BY

Nibir Mandal,  
Jadavpur University, India

## REVIEWED BY

Chun Zhu,  
Hohai University, China  
Manaska Mukhopadhyay,  
The University of Tokyo, Japan

## \*CORRESPONDENCE

Hu Si,  
✉ [sihu@cqu.edu.cn](mailto:sihu@cqu.edu.cn)

RECEIVED 01 October 2024

ACCEPTED 27 January 2025

PUBLISHED 17 February 2025

## CITATION

Liu H, Si H, Yang Z and Xu D (2025) The activation and slip of laboratory faults containing gypsum gouge under triaxial stress conditions.

*Front. Earth Sci.* 13:1504605.

doi: 10.3389/feart.2025.1504605

## COPYRIGHT

© 2025 Liu, Si, Yang and Xu. This is an open-access article distributed under the terms of the [Creative Commons Attribution License \(CC BY\)](https://creativecommons.org/licenses/by/4.0/). The use, distribution or reproduction in other forums is permitted, provided the original author(s) and the copyright owner(s) are credited and that the original publication in this journal is cited, in accordance with accepted academic practice. No use, distribution or reproduction is permitted which does not comply with these terms.

# The activation and slip of laboratory faults containing gypsum gouge under triaxial stress conditions

Han Liu<sup>1,2</sup>, Hu Si<sup>1,2\*</sup>, Zili Yang<sup>1,3</sup> and Dayang Xu<sup>1,4</sup>

<sup>1</sup>State Key Laboratory of Coal Mine Disaster Dynamics and Control, Chongqing University, Chongqing, China, <sup>2</sup>School of Resources and Safety Engineering, Chongqing University, Chongqing, China, <sup>3</sup>CETC Academy of Chips Technology, Chongqing, China, <sup>4</sup>Jiujiang University, School Architecture Engineering and Planning, Jiujiang, China

Understanding the activation and slip characteristics of faults is essential for the safety and stability of underground engineering. The mechanical behavior of laboratory faults with gouge of specific strength remains unclear. Therefore, triaxial compression tests were performed on saw-cut sandstone specimens containing artificial gypsum gouge. Strength criteria analysis, crack pattern analysis, and fault surface roughness evaluation were conducted to investigate the effects of dip angle, confining pressure, and loading rate on the failure modes and stick-slip characteristics of the faults. The results indicate that as the fault dip increases, the fracture mode transitions from rock damage to shear failure along the saw-cut surface. Fractures within the gypsum fault gouge result in deviations between the measured and theoretical strength values. The magnitude of the normal stress controls the fault surface roughness and the variations in the stress drop during fault activation. An increase in the loading rate results in a transition from stick-slip behavior to stable slip. This study enhances the understanding of fault stability and provides valuable insights into monitoring strategies for underground engineering and earthquake prediction.

## KEYWORDS

fault strength, fault activation, STICK-SLIP, fault gouge, triaxial loading

## 1 Introduction

Faults, as common geological structures in the Earth's crust, can be observed in rocks ranging from microscopic to outcrop scale (Zhu et al., 2024), aligned in different orientations and at varying depths (Wu et al., 2023). The stability of faults is highly correlated with geologic hazards such as landslides (Li et al., 2024a), rockbursts (Bai et al., 2022), and mudslides (Zhang et al., 2024). Therefore, the study of fault-containing rocks is crucial for the safe development of underground projects (Zhu et al., 2022).

The Amonton-based friction law states that when the shear stress on the fault surface exceeds the critical shear strength, the fault reactivates and slips (Sibson, 1985). However, the differential stress required for fault activation is related to the friction on the fault surface (Ban et al., 2023). This stress is also influenced by the direction of the maximum principal stress (Giorgetti et al., 2019) and the magnitude of the effective stress (Delle Piane et al., 2016). As the fault approaches the critical stress, both normal and shear stresses decrease significantly (Wu et al., 2017). Microscopically, this is associated with a reduction in intergranular forces and particle contact fracture. (Zhang et al., 2023). Oscillation of normal

stress (Yu et al., 2024) and the ratio of normal stress to shear stress (Li et al., 2024b) are associated with the destabilizing fault slip. Unloading of normal stress (Liu et al., 2024) triggered by engineering perturbations such as underground mining and tunneling (Ji et al., 2019) can lead to the sudden activation of faults, causing an extremely strong subsurface dynamic hazards (Niu et al., 2024). Additionally, water injection processes, such as geothermal mining (Ji et al., 2022) and hydraulic fracturing to increase seams (Yaghoubi et al., 2022) can activate faults and induce earthquakes (Wang et al., 2024), by increasing the effective stress on the fault surface (Wynants-Morel et al., 2021). Also, rupture instability is also associated with changes in the direction of principal stresses relative to the direction of rupture (Zhang and Sanderson, 2001).

The stick-slip mechanism observed in laboratory rocks is thought to be similar to the sliding behavior of *in-situ* faults (Brace and Byerlee, 1966). Many laboratory-based fault studies have been conducted to reveal the mechanisms of fault slip and its mechanics (Bolton et al., 2022). Since *in-situ* faults are not zero-thickness planes and contain a range of fault gouge (Choi et al., 2016), the method of filling fault gouge is commonly used to model their friction behavior (Nilsen, 2021). Specifically, commonly used *in-situ* fault gouges in the laboratory, such as those composed of low-strength clay minerals (e.g., clays and layered silicates), tend to exhibit velocity enhancement and stable sliding (Ruggieri et al., 2021). In contrast, the friction coefficients of faults composed of slightly stronger granular minerals (e.g., quartz) decrease with velocity, experiencing unstable stick-slip (Leeman et al., 2016). Additionally, a smaller grain size distribution of fault gouge contributes to fault destabilization as well as strength recovery (Cao et al., 2024). Different mineral compositions affect the frictional strength and rate-dependence of faults (Zhang et al., 2019). The presence of fluids within the gouge layer contributes to stabilizing slip behavior and fault compaction (Kang et al., 2024). Moreover, an increase in temperature promotes the transition of fault gouge from brittle to ductile (Mei et al., 2024). The frictional strength and sliding stability of faults are also controlled by the interaction of several of these factors (An et al., 2021). However, in the vicinity of the fault core, there exist a damage zone with some cohesion (Ben-Zion and Sammis, 2003). As a geological material commonly stronger than clay minerals (Wu et al., 2022), comparative experiments between gypsum and clay mineral gouge (Wu et al., 2022) have demonstrated that gypsum exhibit a stronger tendency to weaken at higher velocities (Ren, 2024). Furthermore, the fault slip behavior observed on gypsum fault gouge is consistent with numerical models and theories applied to natural and induced earthquakes (Buijze et al., 2021). Moreover, the triaxial shear experiment more closely to the simulates the *in-situ* stress of the original rock in the subsurface (Zhong et al., 2023) compared to the direct shear experiment, which applies an inconsistent normal loads to the fault (Ji et al., 2022). Therefore, based on the observations from the aforementioned studies, the following questions warrant further investigation: How does a fault gouge of specific strength affect the fracture pattern of rock specimens? How do factors such as fault dip angle, confining pressure in triaxial tests, and loading rate influence fault activation and slip?

This study primarily investigates the stress-strain characteristics of faults with varying dip angles, as well as the activation and slip behavior of faults under different confining pressures and loading

rates. Incorporating the analysis of fault surface roughness, the study further explores the mechanisms by which gypsum faults influence the strength of sandstones, the transformation of stress drop characteristics during fault activation, and the changes in fault slip patterns. Finally, the study analyzes the correlation between the research results and underground engineering near the faults.

## 2 Materials and methods

### 2.1 Sample selection and treatment

The sandstone used in these experiments is a typical rock from the earthquake-prone Longmenshan Fault Zone of the Sichuan Basin, China (Wang et al., 2014; Long et al., 2022). To ensure the samples had comparable structural properties, cylindrical sandstone samples were cored from individual sandstone blocks along a direction perpendicular to the laminae. The ends of each cylindrical rock sample were carefully ground to a height of 100 mm and a diameter of 50 mm.

The complete sandstone samples were sawed from the center at angles of 0°, 15°, 30°, 35°, 40°, 45°, 50°, 55°, 60°, and 65° relative to the direction of  $\sigma_3$  (Figure 1B). The saw-cut surface was polished using 320-grit sandpaper to ensure uniform surface roughness. The gypsum fault was created by mixing 10  $\mu\text{m}$  bassanite powder with water in a 3:1 ratio, then filling the mixture into the saw-cut surface. The saw-cut surface was then compacted to ensure the gypsum layer thickness was 2 mm. After the bassanite powder rehydrates, it re-bonds the saw-cut surfaces. The specimen was left undisturbed under room temperature and atmospheric pressure for 2 days. The end surfaces of the samples were then checked for flatness. If the maximum height difference were less than 0.05 mm (Cvitanovic et al., 2015), the specimen was prepared for testing. In addition to the saw-cut samples, standard cylindrical gypsum specimens, consistent with the way as the gypsum faults, and standard sandstone specimens were fabricated for mechanical testing. Two samples were prepared under different test conditions to minimize the effect of sample heterogeneity on the experimental results.

### 2.2 Test equipment and procedures

Triaxial tests were performed at room temperature using a servo-controlled MTS815 tester without any pore pressure (Figure 1A). The confining pressure was applied through silicone oil in the triaxial cell. The sample was wrapped with a polyolefin sleeve to separate it from the silicone oil. Axial forces were measured using force transducers with a maximum load capacity of 2200 kN and an accuracy of  $\pm 0.5\%$ . Circumferential strain  $\epsilon_r$  was consecutively measured using circumferential extensometers with a measuring range of +12.5 mm, -2.5 mm, and an accuracy of  $\pm 0.5\%$ .

Uniaxial and triaxial compression tests were first performed on gypsum and sandstone standards, followed by triaxial compression tests on sawed samples. The experimental procedure is as follows: First, the confining pressure was applied at a rate of 2 MPa/min until it reached the set value of 10 MPa. The confining pressure was then kept constant, and the axial load was applied at a fixed displacement

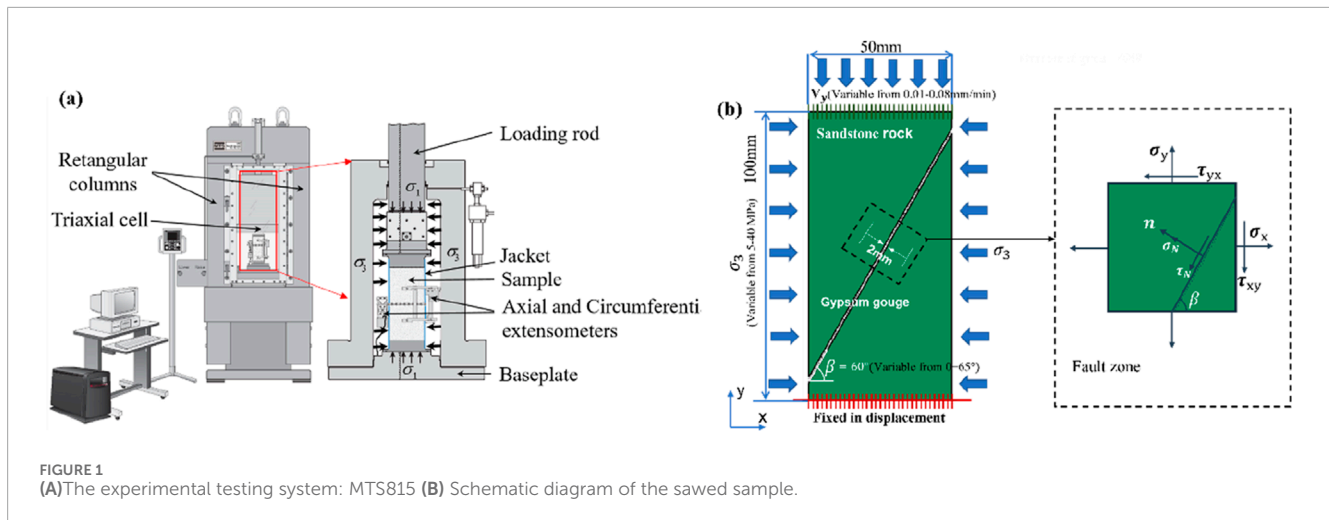


FIGURE 1 (A) The experimental testing system: MTS815 (B) Schematic diagram of the sawed sample.

rate of 0.01 mm/min, corresponding to a strain rate of approximately  $1.67 \times 10^{-6} \text{ s}^{-1}$ . The procedure was terminated when the specimen deformation gradually stabilized. After the tests on saw-cut samples with different dip angles, additional tests were conducted on  $60^\circ$  saw-cut samples under various confining pressures (5, 10, 20, 40 MPa) and at different loading rates ( $5\text{E}^{-3}$ ,  $1\text{E}^{-2}$ ,  $2\text{E}^{-2}$ ,  $4\text{E}^{-2}$ ,  $8\text{E}^{-2}$  mm/min) under a constant confining pressure of 10 MPa. At the end of the experiment, the surface morphology of the fault was reconstructed using a non-contact tomography scanner, and the roughness of the surface fracture was analyzed.

### 3 Results

In the following analysis and discussion, the maximum principal stress is denoted as  $\sigma_1$ , and the minimum principal stress as  $\sigma_3$ . The differential stress  $\sigma_d$  is calculated as the axial stress ( $\sigma_1$ ) minus the confining pressure ( $\sigma_3$ ):  $\sigma_d = \sigma_1 - \sigma_3$ .  $\beta$  is the angle between the fault and  $\sigma_3$  direction, and  $P_c$  is the confining pressure applied during the test.  $\sigma_d^{max}$  is the maximum stress drop during the stick-slip stage. The calculation of the shear stress  $\tau_N$  and normal stress  $\sigma_N$  on the fault plane is given by the following Formula 1. Compressive stresses and strains are positive in the sign convention.

$$\left. \begin{aligned} \sigma_N &= \frac{1}{2}(\sigma_1 + \sigma_3) + \frac{1}{2}(\sigma_1 - \sigma_3) \cos 2\beta \\ \tau_N &= \frac{1}{2}(\sigma_1 - \sigma_3) \sin 2\beta \end{aligned} \right\} \quad (1)$$

#### 3.1 Fundamental mechanical characteristics of sandstone specimens and gypsum faults

The stress-strain curves provide valuable insights into the evolution of the mechanical properties of the specimens under loading. Table 1 shows the basic physical properties of the sandstone and gypsum used in this laboratory test. Figure 2A presents the uniaxial compressive stress-strain curves of intact sandstone and

gypsum specimens. The fractures of both sandstone and gypsum exhibit typical brittle characteristics. The uniaxial compressive strength of sandstone is 67.22 MPa, approximately 3.3 times that of gypsum. The elastic modulus of gypsum is 1.7 GPa, which is much smaller than that of sandstone (10.52 GPa). The deformation of gypsum specimen during the initial stage of pore compaction is significantly larger than that of sandstone specimen due to its higher porosity. Figure 2B shows the differential stress-strain curves of  $60^\circ$  saw-cut samples with and without gypsum faults. Due to the consolidating effect of gypsum, specimens with gypsum faults exhibit significantly higher shear strength compared to those without gypsum. Moreover, the specimen with a gypsum fault undergoes stick-slip behavior upon activation, while the specimen without a gypsum fault undergoes stable sliding after activation.

#### 3.2 Mechanical characteristics of gypsum faults

##### 3.2.1 Gypsum faults with varying dip angles

For better classification and understanding, the results are divided into two groups: the  $0^\circ$ – $40^\circ$  group (Figure 3A), where brittle fracture occurs, and the  $45^\circ$ – $65^\circ$  group (Figure 3B), where stick-slip dominates. Table 2 presents the strength and Young's modulus values of intact rock specimen and saw-cut specimens at different  $\beta$  angles under a  $P_c$  of 10 MPa.

From Figure 3A, it can be observed that saw-cut specimens undergo several stages in the differential stress-strain curve: closure of initial porosity, elastic loading, progressive yielding, and one or more stress drops until specimen failure. Gypsum faults significantly affect the mechanical strength of sandstone, with increasing  $\beta$  angles causing a continuous decline in specimen strength (Table 2). In  $\beta$  range of  $15^\circ$ – $40^\circ$ , specimens may exhibit multiple stress drops during the failure stage. At  $\beta$  angles of  $35^\circ$ ,  $40^\circ$ , several stress drops occur during the elastic loading stage. However, the overall stress continues to rise, eventually causing specimen failure. In the  $\beta$  range of  $45^\circ$ – $65^\circ$  (Figure 3B), after fault activation, the differential stress exhibits periodic variations. At  $\beta$  angle of  $45^\circ$ , a significant stress drop, similar to brittle failure, occurs at fault activation, followed

TABLE 1 Physical properties of sandstone and gypsum.

Rock material	Items						
	Density	Uniaxial compressive strength	Elastic modulus	Poisson ratio	Porosity	Cohesion	Internal friction angle
Sandstone	2.55 (g • cm <sup>-3</sup> )	67.22 MPa	10.5 GPa	0.23	8.02%	18.3 MPa	32°
Gypsum	1.82 (g • cm <sup>-3</sup> )	20.43 MPa	1.7 GPa	0.13	30.8%	5.7 MPa	30°

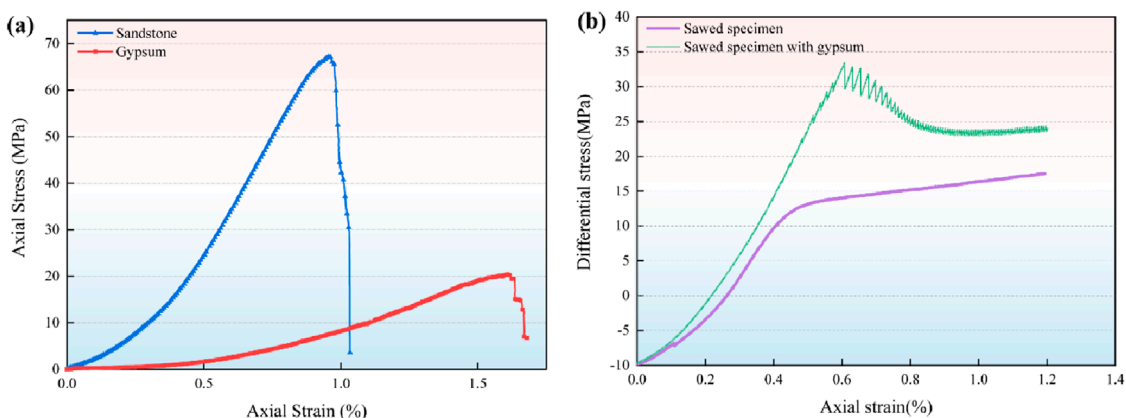


FIGURE 2 (A) Uniaxial compressive strength of sandstone and gypsum standard specimens (B) Differential stress-strain curves of saw-cut specimens with and without gypsum.

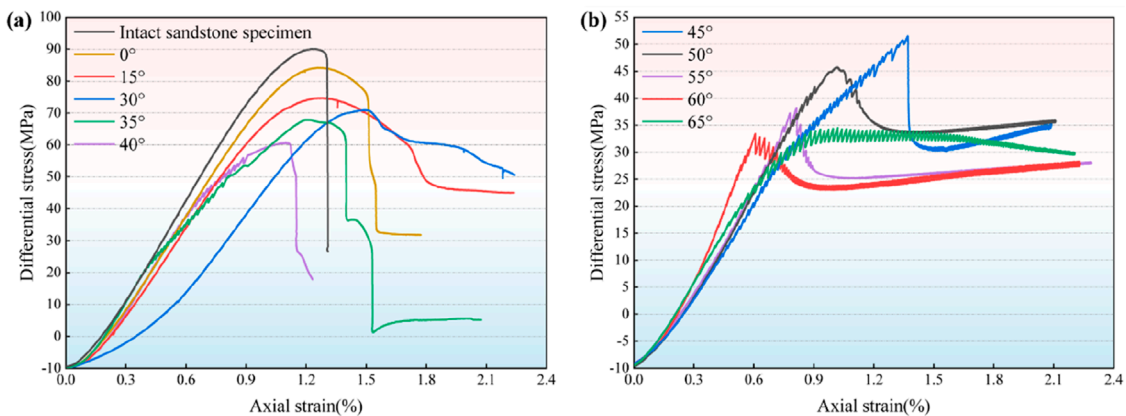


FIGURE 3 Differential stress-strain curves of sandstone specimens containing gypsum gouge at different dip angles, grouped by (A) 0°–40° (B) 45°–65°.

TABLE 2 Physical properties of specimens with faults at different dip angle.

Items	Intact rock	Dip angle of faults									
		0°	15°	30°	35°	40°	45°	50°	55°	60°	65°
Strength (MPa)	100.2	94.2	84.7	80.7	77	70	61.0	55.5	48.8	45.0	45.2
Young's modulus (GPa)	10.0	9.7	8.8	8.4	8.1	7.8	9.3	9.4	9.1	10.3	7.7

TABLE 3 Stress characteristics during stick-slip of samples under different confining pressure.

Confining pressure	Shear strength (MPa)	Stress in stick-slip (MPa)	Overall stress drop (MPa)
5 MPa	21.76	9.4	12.36
10 MPa	43.42	23.7	19.72
20 MPa	65.3	31.7	33.6
40 MPa	113	38.4	74.6

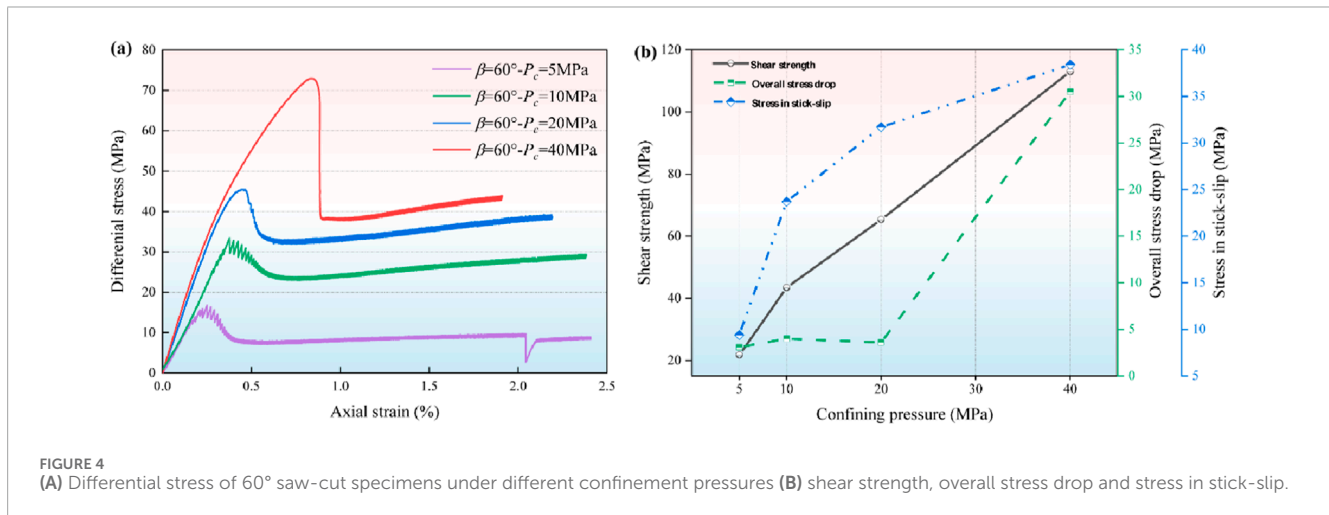


FIGURE 4

(A) Differential stress of 60° saw-cut specimens under different confinement pressures (B) shear strength, overall stress drop and stress in stick-slip.

by periodic stick-slip. As the  $\beta$  increases from 45° to 60°, the stress drop behavior at fault activation gradually shifts from “sudden” to “periodic”. At  $\beta$  angle of 65°, there is no decrease in the average stress value at fault activation.

### 3.2.2 Gypsum faults under varying confining pressure

Based on the previous analysis, we know that the differential stress is smallest when fault undergoes stable stick-slip at  $\beta$  angle of 60°. This can be considered the optimal dip angle for gypsum fault slip. Based on this, to study the effect of confining pressure on gypsum faults, we conducted further tests at  $\beta$  angle of 60° under  $P_c$  of 5, 10, 20, and 40 MPa.

The measured and calculated values of specimen shear strength, overall stress drop at activation, and average stress during stick-slip are listed in Table 3, all of which increase with the rise in confining pressure (Figure 4B). It is noteworthy that, similar to the variation in the  $\beta$  range of 45°–65°, with the increase in  $P_c$ , the stress drop after activation gradually transitions from “periodic oscillation drop” to “sudden drop” (Figure 4A). The two similar trends under different  $\beta$  angles and  $P_c$  may be related to the stress state on the fault surface, which warrants further detailed investigation in subsequent studies.

### 3.2.3 Gypsum faults under various loading rates

Based on the previous analysis, gypsum faults undergo a fixed cycle of stick-slip after reaching the peak. To investigate whether different loading rates affect the fault slip behavior. The fault was loaded to the stick-slip stage at a loading rate of  $2E^{-2}$  mm/min at  $\beta$  of

60° and  $P_c$  of 10 MPa, and then the loading rate was increased from  $5E^{-3}$  mm/min to  $8E^{-2}$  mm/min, with each increment loading 0.3% strain value, as shown in Figure 5A.

With the increase in loading rate, the stress drop during fault stick-slip gradually decreases from 0.9 MPa to 0.1 MPa, and cycle time for single stick-slip decreases from 28s to 8s (Figure 5B). When the loading rate reaches 0.08 mm/min, no apparent stress drop occurs, indicating that the fault no longer exhibits stick-slip behavior and has entered a “stable-slip” state. Therefore, an increase in the loading rate transitions the fault slip from “stick-slip” to “stable-slip.” When the stiffness of the sandstone and gypsum fault system is lower than the fault slip weakening rate (Ji et al., 2019), the fracture will undergo dynamic slip. Thus, for faults with loading rates between  $5E^{-3}$  and  $4E^{-2}$  mm/min, the lower slip weakening rate causes the fault to undergo periodic stick-slip. In contrast, at  $8E^{-2}$  mm/min, the slip rate of the fault is primarily influenced by the load point rate of the testing machine, resulting in stable slip.

## 3.3 Fracture patterns of saw-cut specimens

Figure 6 illustrates the fracture morphology and types of cracks after the failure of intact rock and saw-cut specimens. All specimens containing gypsum faults suffered severe damage; however, the fractures in sandstone varied significantly with different  $\beta$  angles (Figure 6A). For intact sandstone, it primarily exhibits brittle cracks at an angle of approximately 72° to  $\sigma_3$  direction. In contrast, the fractures of specimens at  $\beta$  of 0°, 15° are similar to those

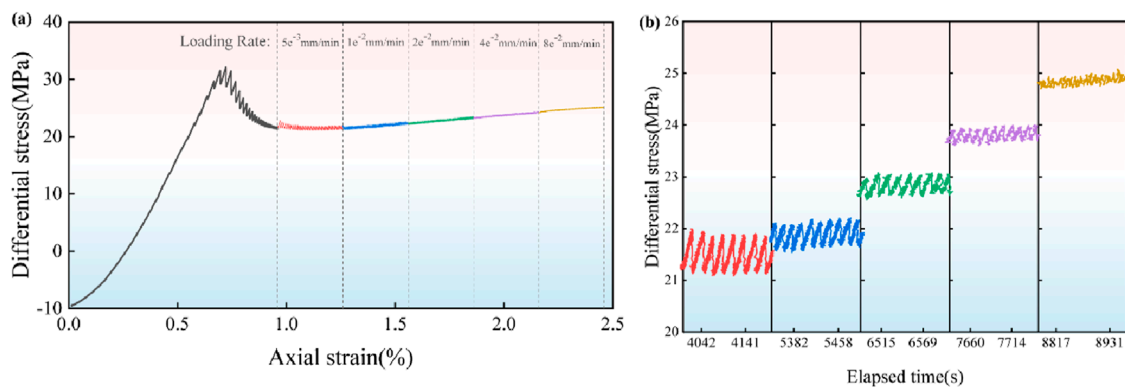


FIGURE 5  
(A) Differential stress of specimens at various loading rates (B) Amplified plot of differential stress.

of intact sandstone, with macroscopic cracks traversing the fault, however, the fracture angles decrease to approximately  $60^\circ$  and  $50^\circ$ , respectively (Figure 6B). Fractures originate from tensile wing-shaped cracks starting from the saw-cut surface, extending to both sides, and eventually intersecting with symmetric cracks on the back of the specimen. In specimens at  $\beta$  of  $30^\circ$ ,  $35^\circ$ , the angle between the main crack and the saw-cut surface further decreases to approximately  $30^\circ$  and  $20^\circ$ , respectively. No main cracks were observed on the surfaces in specimens of  $\beta$  between  $45^\circ$  and  $65^\circ$  (Figure 6A). At the  $\beta$  of  $45^\circ$ , microcracks were observed in the rocks on both sides of the fault. Meanwhile, fractures within the gypsum fault were observed at  $\beta$  of  $45^\circ$ ,  $50^\circ$ , and  $65^\circ$ , which may be related to the deviation from the optimal dip angle for fault slip, leading to shear cracks within the gypsum fault (Figure 6C). In contrast, at the  $\beta$  of  $55^\circ$ ,  $60^\circ$ , no microcracks were observed in the rocks on both sides of the fault, and no fracturing occurred within the gypsum fault. The gypsum fault completely separated from the sandstone matrix on one side and slid along the contact surface between the two (Figure 6C).

### 3.4 Morphology of the fault surface

The statistical parameters are commonly used to evaluate the morphology of rock fractures or sawed surfaces can be directly derived from the data coordinates of the asperities on the fracture surface. The statistical parameters typically include the root mean square of the height of the profile  $R_q$  (Equation 2), the peak asperity height  $R_z$  (Equation 3) in the amplitude characteristics; and the root mean square of the first derivative of the profile  $Z_2$  (Equation 4).

$$R_q = \left[ \frac{1}{N} \sum_{i=1}^N (z_i - z_a)^2 \right]^{\frac{1}{2}} \quad (2)$$

$$R_z = z_{max} - z_{min} \quad (3)$$

$$Z_2 = \left[ \frac{1}{N-1} \sum_{i=1}^{N-1} \frac{(z_{i+1} - z_i)^2}{(x_{i+1} - x_i)^2} \right]^{\frac{1}{2}} \quad (4)$$

where  $z_i$  represents the surface height at point  $i$ ,  $N$  is the number of sampling points,  $z_a$  is the distance between the profile and the

mean elevation line,  $z_{max}$  is the maximum surface height,  $z_{min}$  is the minimum surface height, and  $(x_i, z_i)$  and  $(x_{i+1}, z_{i+1})$  are the coordinates of the two adjacent points on the fracture profile. In addition, the Joint Roughness Coefficient (JRC) is calculated using an empirical formula (Tse and Cruden, 1979):

$$JRC = 32.2 + 32.47 \log Z_2 \quad (5)$$

In order to calculate the statistical roughness parameter and JRC (Equation 5), 26 equally spaced fracture profiles were extracted from each fault surface along the direction parallel to the fault. The average roughness parameters and JRC for the 26 profiles are listed in Table 4.

After experiments, both sandstone layer and gypsum layer were subjected to non-contact tomography scanner and reconstruction (Figure 7). In addition to the surface cracks mentioned earlier, it was also observed that the surface of the gypsum was significantly smoother than that of the sandstone, attributed to the differing grain sizes of the sandstone and gypsum particles. This was corroborated by the roughness calculations (Table 4). A clear slicken line was observed parallel to the slip direction on the surface of the sandstone layer, which occurred due to the fracture and displacement of asperities on the sandstone layers. Its visibility increased with higher  $P_c$  or lower  $\beta$  angle, which is related to the stress state on the fault surface, and will be discussed in more detail. The roughness of the fracture surface was significantly greater than that of the shear surface (Figure 8A), with the complete inter-rock fracture particularly triggered by the  $0^\circ$  fault. As  $P_c$  increases, it was observed that the roughness of the gypsum layer decreases, while the roughness of the sandstone layer increases (Figure 8B). This occurs because the deformation modulus of the gypsum layer is greater, and compaction under high normal pressure reduces the asperity height of the gypsum layer. The fracture and displacement of asperity on the sandstone surface increased the roughness.

The differences in fault surface morphology are closely related to the fracture and stick-slip patterns of the fault. In the following sections, we will discuss in detail the impact of fault dip on shear strength of saw-cut specimens, as well as the mechanisms of confining pressure and loading rate on the stick-slip state of the fault. The correlation of experimental results with underground engineering near *in-situ* faults is also discussed.

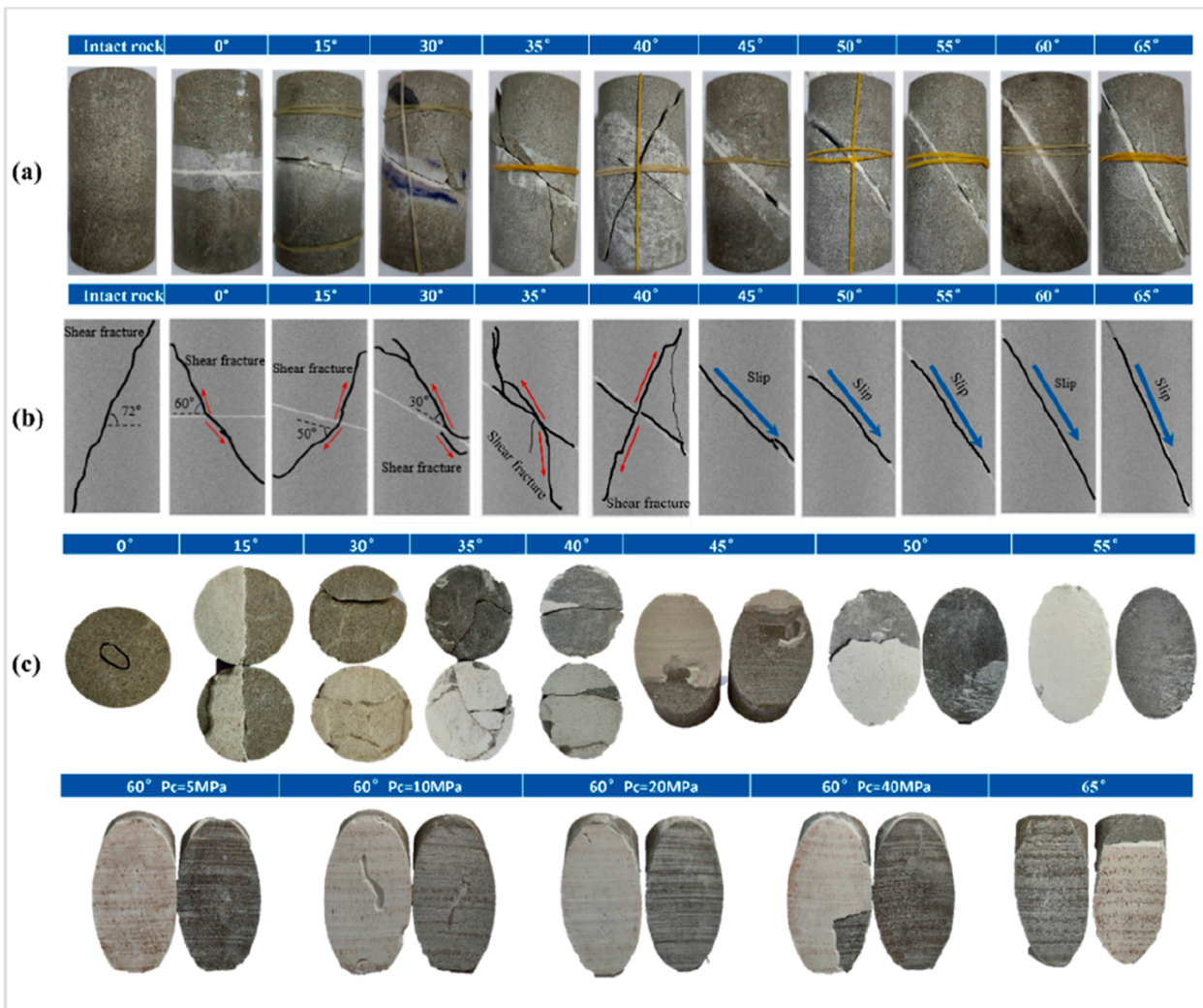


FIGURE 6 (A) Crack morphology on the surface of saw-cut specimens (B) Crack types in saw-cut specimens (C) Cracks morphology on gypsum fault and saw-cut surfaces.

## 4 Discussion

### 4.1 The impact of gypsum faults on the strength of sandstone

Based on the relationship between shear stress and normal stress components on the fault surface under different  $P_c$  for the 60° fault (Figure 1B), we fitted the friction coefficient and cohesion of the contact surface with gypsum faults (Figure 9A). According to the single structural plane strength criterion (Jaeger, 1960), when the fault dip angle is equal to  $= 45^\circ + \gamma/2$  [ $\gamma = 90^\circ - \tan^{-1}(1/\mu)$ ], i.e.,  $\beta = 58^\circ$ , this represents the optimal dip angle for fault slip. When  $\beta_1(36^\circ) < \beta < \beta_2(80^\circ)$ , the specimen will slip along the fault plane. When the fault dip angle is outside this range, the maximum differential stress of the rock containing the fault equals that of the intact rock. This value can be obtained through the internal friction angle  $\varphi$  and cohesion  $c_0$  of the rock matrix (Table 1), as given by Equation 6:

$$\sigma_d = \frac{2c_0 \cos \varphi + 2\sigma_3 \sin \varphi}{1 - \sin \varphi} \quad (6)$$

For a fault containing cohesive fault gouge (Fagereng et al., 2010), the maximum differential stress required for its activation is:

$$\sigma_d = [( \tan \beta + \cot \beta ) / ( 1 - \mu \cot \beta )] [ c_w + \mu \sigma_3 ] \quad (7)$$

Where  $\sigma_3$  is the minimum principal stress,  $\mu$  is the friction coefficient of pre-existing fractures,  $\beta$  is the fracture angle relative to  $\sigma_3$ ,  $c_w$  is the cohesive strength of the fault gouge.

Therefore, based on Equations 6, 7, we can calculate and predict the differential stress at failure for rocks containing cohesive faults (Figure 9B). Within  $\beta$  ranging from 0° to 40°, the maximum differential stress in saw-cut specimens decreases gradually as increasing  $\beta$  angle from experimental observations. The presence of gypsum layers with finite thickness, unlike the theoretical assumption of infinitesimally thin faults, alters the mechanical properties of the sandstone. In  $\beta$  of 0°–30°, since the cohesive

TABLE 4 The roughness parameters and JRC of different fault surfaces.

Fracture surface	Sandstone layer				Gypsum layer			
	$R_q$	$R_z$	$Z_2$	JRC	$R_q$	$R_z$	$Z_2$	JRC
0°	9.564	58.018	0.527	23.180	10.269	54.243	0.574	24.380
15°	1.368	19.036	0.494	22.260	1.152	4.378	0.164	6.690
30°	0.479	41.273	0.216	10.590	0.829	4.068	0.216	10.610
35°	0.430	9.065	0.322	16.210	0.296	8.398	0.245	12.370
40°	1.217	8.114	0.210	10.170	0.495	5.896	0.160	6.390
45°	0.331	2.506	0.196	9.250	0.802	2.635	0.168	7.030
50°	0.055	0.613	0.212	10.340	0.216	1.721	0.153	5.680
55°	0.045	0.762	0.156	6.030	0.050	0.547	0.149	5.310
60° $P_c = 5$ MPa	0.053	0.502	0.143	4.740	0.059	0.519	0.184	8.330
60° $P_c = 10$ MPa	0.041	0.699	0.202	9.630	0.150	0.815	0.156	6.010
60° $P_c = 20$ MPa	0.065	0.651	0.204	9.810	0.071	0.840	0.128	3.240
60° $P_c = 40$ MPa	0.051	0.680	0.235	11.750	0.065	0.694	0.127	3.050
65°	0.043	0.836	0.153	5.760	0.055	1.241	0.134	3.810

strength of the gypsum is significantly lower than that of the sandstone, the presence of gypsum fault changes the overall cohesion of the saw-cut specimen and affects the friction angle during failure, resulting in cracks through the gypsum layer having angles lower than the internal friction angle of intact sandstone specimens (Figure 6). In  $\beta$  at 35° and 40°, closer to the optimal slip angle for fault activation, the fault locking effect of the faults is unstable. For instance, during the linearly increased stage of the specimen under stress, some slight stress drops were observed, indicating sliding between the fault surfaces. In  $\beta$  ranging from 45° to 65°, the deviation between theoretical predictions and experimental results may be attributed to the rotation of stress within the gypsum faults (Giorgetti et al., 2019). This is influenced by the variation between the direction of maximum shear stress and  $\beta$  angle, with internal cracks within the fault corroborating this observation (Figure 7). Compared to unfilled saw-cut samples (Guerin-Marthe et al., 2023; Meng et al., 2023) or saw-cut samples with fault clay gouge (Giorgetti et al., 2019), the presence of internal cracks within the gypsum faults at 45° and 50° indicates that the sliding surface is not a two-dimensional plane. Faults slide along newly formed surfaces, increasing the roughness between faults and consequently increasing the friction coefficient. Thus, this alters the distribution of shear and normal stresses on the fault surfaces, requiring a higher differential stress for fault activation.

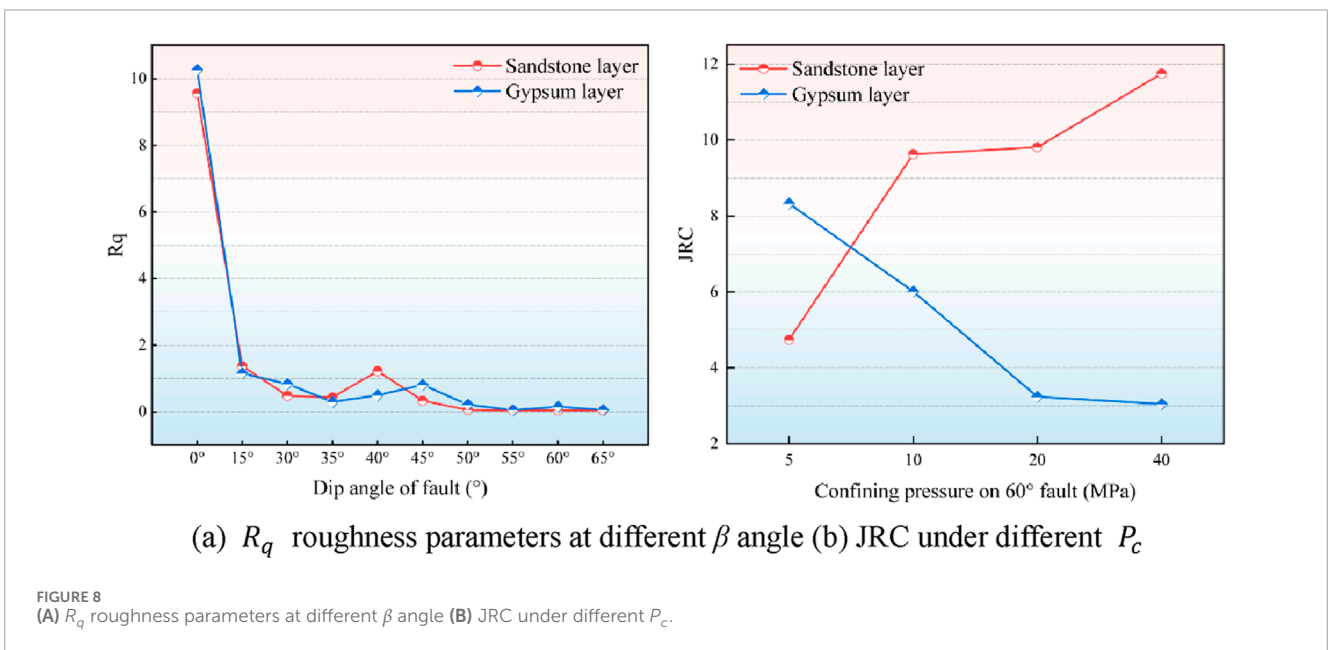
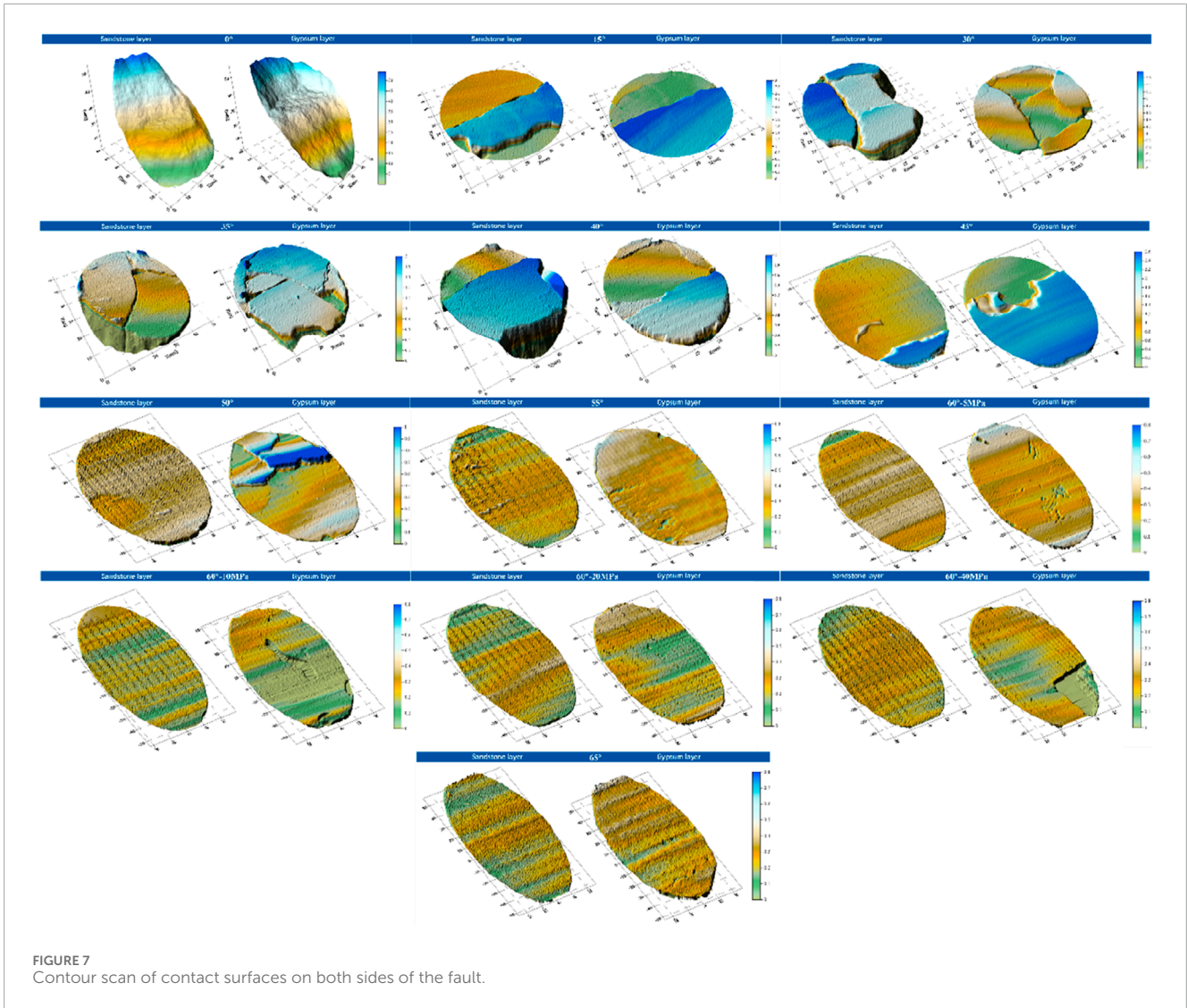
## 4.2 The transformation of stick-slip mode during activation

Based on the previous analysis,  $\beta$  exceeding 40° consistently exhibit a fixed amplitude of stick-slip behavior. However, the

trends in differential stress before and after fault activation vary. Importantly, the differential stress trends under different  $P_c$  closely resemble those  $\beta$  of 45°–60°. The differential stress during this stage was extracted (Figure 10). The figures identify four main modes of stick-slip from fault activation. These modes are: Type 1, depicted in Figures 10A, E, featuring a sharp drop at fault activation; Type 2, shown in Figures 10B, F, featuring a slow decrease with irregular multi-peak behavior at fault activation; Type 3, illustrated in Figures 10C, G, H displaying a cyclic decrease around fault activation; and Type 4, shown in Figure 10D, demonstrating a cyclic and steady decrease around fault activation.

The characteristics of stress drop during fault activation are correlated with the stress field distribution on the fault plane. Under lower  $\beta$  or higher  $P_c$ , the fault plane commonly exhibits higher normal stress. The interlocking effect between the gypsum fault crack and the sandstone layer results in static friction significantly exceeding sliding friction. Higher normal stress leads to tighter contact between the surfaces, resulting in stronger adhesion and interlocking of rough particles, thereby increasing the static friction coefficient. The combined increase in friction coefficient and normal stress necessitates a higher shear force for fault activation. At the same time, greater shear force accumulates stronger sliding potential energy, increasing the speed of frictional rupture (Brantut et al., 2016). Therefore, a Type 1 or Type 2 stress drop occurs upon fault activation. Influenced by decreasing  $P_c$  or increasing  $\beta$ , the decrease in roughness of the sandstone layer and reduction of normal stresses also cause the fault to transition from dynamic destabilization to progressive fault activation (Type 3). At 65°, lower normal stresses and lower roughness allow static friction to approach sliding friction, thus producing a Type 4 change characteristic.





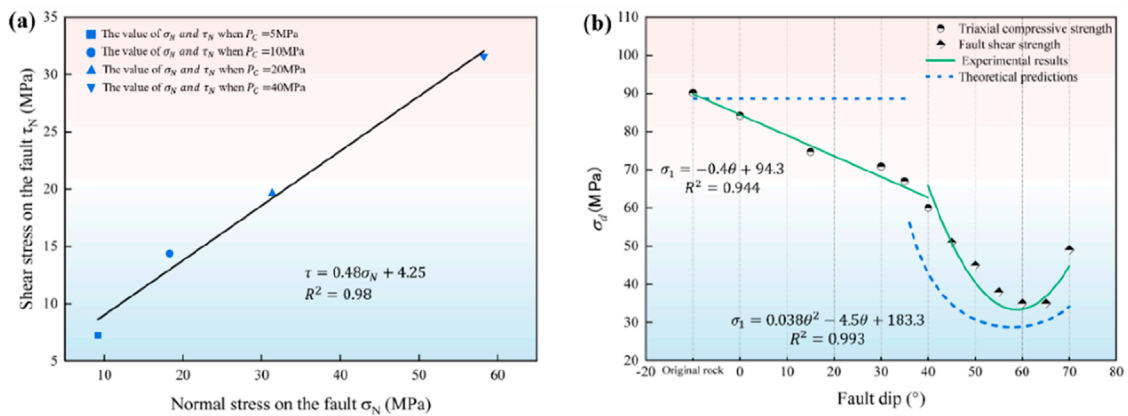


FIGURE 9 (A) Strength fitting curve of the gypsum fault (B) The theoretical and predicted values of the maximum differential stress for gypsum-containing specimens.

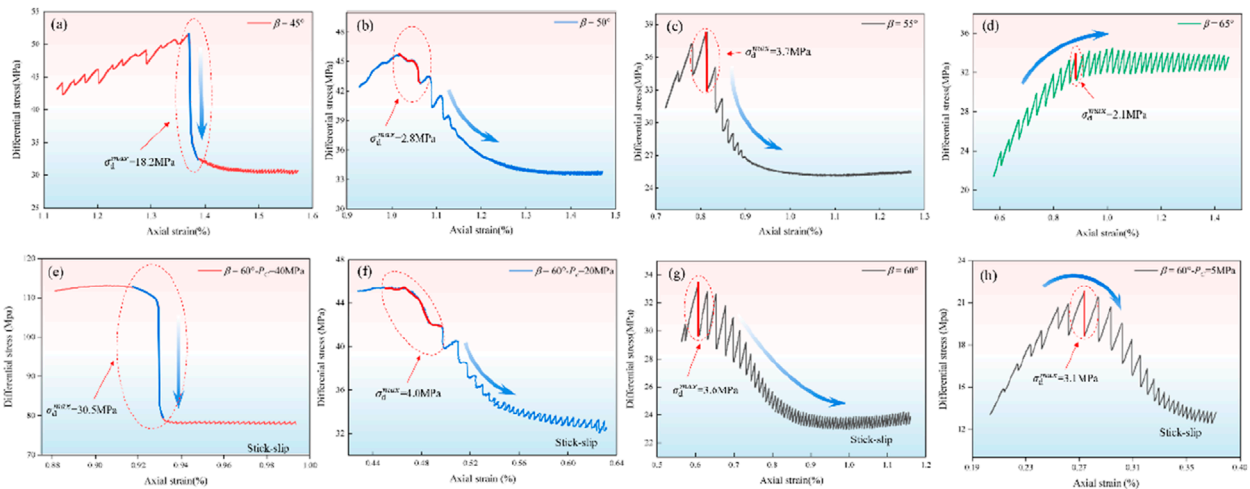


FIGURE 10 Variation in stick-slip types during fault activation under the influence of fault angle grouped by: (A) 45°, (B) 50°, (C) 55°, (D) 65°, (E) 60°. Changes in stick-slip types under the influence of confining pressure grouped by: 5 MPa (H), 10 MPa (G), 20 MPa (F), 40 MPa (E).

### 4.3 Correlation between fault stick-slip and slip rate

The correlation between the rate of faults and stress forms the basis for studying fault instability. During the specimen loading process, the radial deformation of the specimen is mainly influenced by three factors: first, lateral expansion during loading, primarily controlled by the material's inherent Poisson's ratio; second, the main fracture produced by sandstone failure under the influence of low-angle faults, and the deformation caused by continuous opening of fractures; third, the relative sliding between pre-existing faults under the influence of high-angle fault sliding. For  $\beta$  above 45°, the lateral displacement before fault activation is minimal. Therefore, during the fault sliding process, the radial displacement caused by the deformation of sandstone due to the Poisson effect is negligible. Consequently, the change in radial displacement can be

used to reflect the fault slip displacement. For faults in the slip stage, according to the trigonometric relations, the relationship between radial displacement and fault slip is as Equation 8:

$$\Delta s = \frac{\Delta l - 2\pi r}{4 \cos \beta} \tag{8}$$

where  $\Delta s$  is the fault slip displacement,  $\Delta l$  is the circumferential displacement during the slip stage,  $r$  is the radius of the cylindrical sample. The slip rate of the fault is defined as the first derivative of displacement with respect to time. Figures 11A–C present the variations in fault displacement and slip rate during fault sliding processes at different  $\beta$  angles,  $P_c$ , and loading rates, respectively.

Each fault stick-slip event is accompanied by stress drop and acceleration/deceleration of the fault, since there is a positive correlation between fault slip rate and stress drop (Guerin-Marthe et al., 2023). This results in a higher slip rate during fault activation for lower  $\beta$  and higher  $P_c$ . Notably, faults under 40 MPa  $P_c$

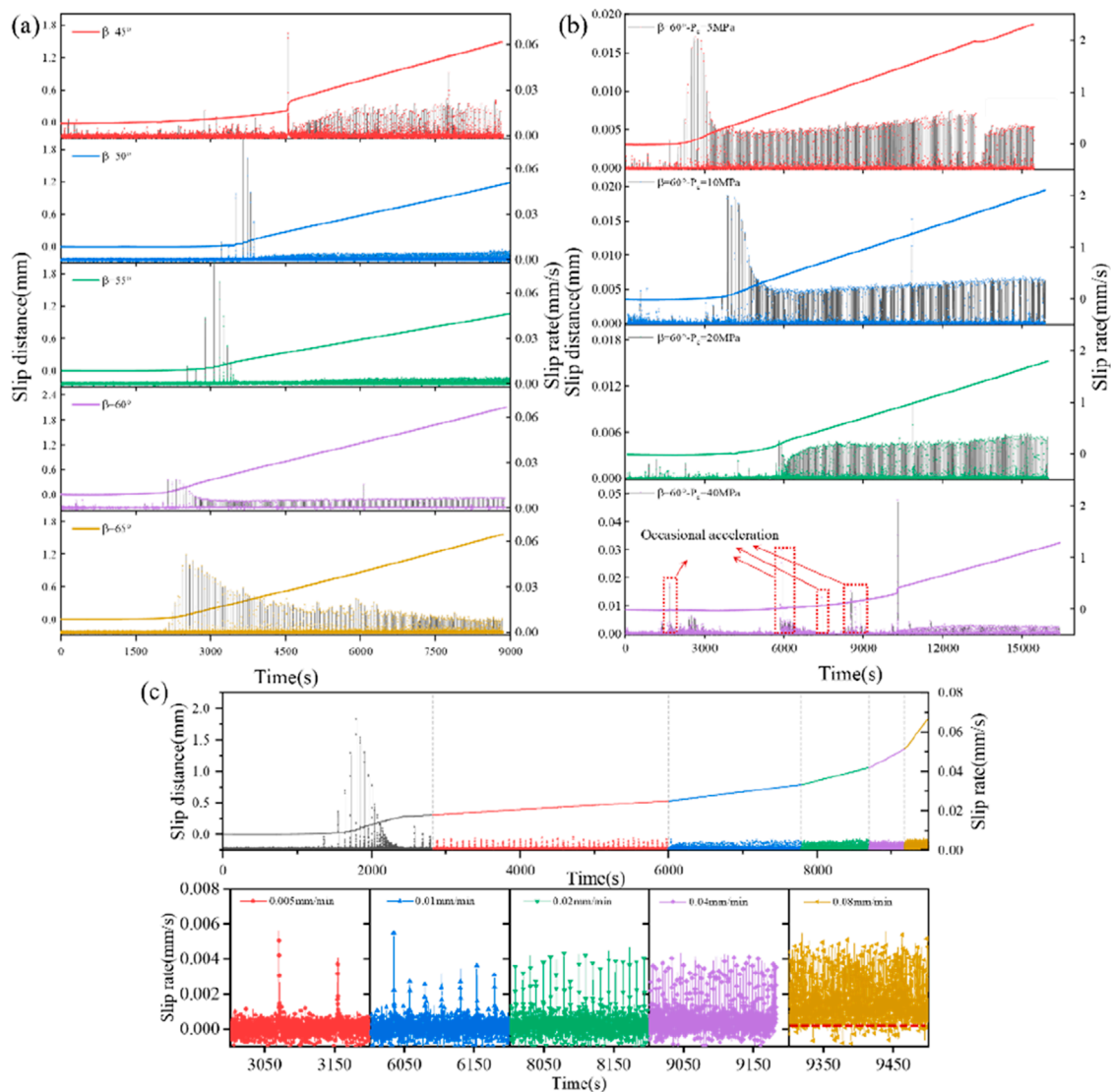


FIGURE 11 Slip rate and displacement of laboratory fault grouped by: various dip angles (A), various confining pressure (B), various loading rate (C).

show several accelerations before complete activation (Figure 11B). This occurs because high  $P_c$  and shear stress can cause localized rupture of asperities, triggering occasional accelerations. For faults under loading rates of  $5E^{-3}$  -  $4E^{-2}$ , although the magnitude of stress drop decreases with increasing loading rate, the average and maximum slip rates remain nearly the same. This indicates that the loading rate primarily influences fault displacement through the stick-slip cycle. When the loading rate reaches  $8E^{-2}$  mm/min, the fault slip rate does not drop to zero (Figure 11C), proving that the fault stops stick-slip and transitions into stable sliding at a certain loading rate. It is likely that as the loading rate continues to increase, the slip rate of the fault becomes primarily associated with the loading rate, and the fault will continue to slide along with the displacement of the platen. The preceding discussion demonstrates that the maximum slip rate of the laboratory fault is mainly controlled by  $\beta$  and  $P_c$ , while the loading rate primarily regulates the stick-slip cycle of the fault.

#### 4.4 Correlation with underground engineering

Although our study was conducted in a laboratory, work on rock damage processes from the laboratory-scale to the Earth-scale is very common (Ke et al., 2018; Xu et al., 2023). Our observations indicate that low-dip faults cause significant stress accumulation within the surrounding rock mass, resulting in increased damage to the rock mass and expanding the extent of the fracture zone around the fault core. This not only reduces the stability of the surrounding rock mass in projects (Su et al., 2017), but also increases the porosity and permeability of the rock mass (Hou et al., 2024), raising the risk of water and mud surges (Zhang et al., 2024) in mines, tunnels and other projects. High-dip faults have a stronger tendency to slip, and sudden fault activation may trigger localized seismic shaking (Cao et al., 2024). In addition, as resource extraction goes deeper (Wang et al., 2017), high confining pressure in deep

can place faults under greater critical stress, which may lead to localized rupture and episodic acceleration. There is also greater rupture velocity when the fault is fully activated. Furthermore, due to the stress field in deep rock masses (Pan et al., 2023), stress redistribution caused by fault destabilization (Ju et al., 2022) lead to dynamic hazards such as rockbursts and coal and gas outbursts (Bai et al., 2022). The laboratory loading rate reflects the construction speed and excavation cycle of underground projects (Liu et al., 2024), and the choice of construction strategies influences the stress and slip states of the fault (Rasouli et al., 2011). Therefore, geological exploration and monitoring should be emphasized in the design and construction of underground engineering. During construction, excavation progress and roadway support design should be adapted to the specific geological conditions. Additionally, emergency measures should be designed and optimized. These measures are essential to ensure the stability of the fault and the safety of the corresponding underground engineering.

## 5 Conclusion

In this study, triaxial compression tests were conducted on sandstone containing gypsum faults. Test conditions with different fault dip angles, confining pressures and loading rates were examined, leading to the following conclusions:

- (1) The dip angle of the fault significantly influences the failure strength and fracture mode of the saw-cut specimens. Specimens with dip angles of 0°–40° mainly fracture along the main crack through the gypsum fault, and the strength decreases linearly with increasing dip angle. Specimens with dip angles of 45°–65° fracture and slip along fractures in both the sandstone plane and the gypsum fault. Fractures within the gypsum fault, along with stress rotation, cause discrepancies between theoretical analysis and measured shear strength values.
- (2) Normal stress magnitude and surface roughness on the fault plane influence the occurrence of four primary stick-slip modes during fault activation. The increase in normal stress causes the roughness of the sandstone layer to increase while that of the gypsum layer decreases, making slicken line on the sandstone layer more prominent.
- (3) The maximum slip rate of a fault is related to the maximum stress drop at activation. The dip angle of faults and confining pressure influence the maximum slip rate. An increase in the loading rate affects the fault stick-slip cycle period, and the slip mode of the fault transitions from stick-slip to stable-slip as the loading rate increases.
- (4) This study emphasizes the impact of fault dip, confining pressure, and loading rate on rock mass stability in underground engineering. Low-dip faults increase damage, porosity, and permeability, while high-dip faults may trigger seismic shaking and rupture more rapidly under higher

confining pressure. Additionally, the loading rate affects the fault's slip state, highlighting the importance of geological monitoring and strategic planning to ensure safety.

## Data availability statement

The original contributions presented in the study are included in the article/supplementary material, further inquiries can be directed to the corresponding author.

## Author contributions

HL: Conceptualization, Data curation, Formal Analysis, Writing–original draft, Writing–review and editing. HS: Conceptualization, Project administration, Resources, Supervision, Writing–review and editing. ZY: Supervision, Writing–review and editing. DX: Conceptualization, Investigation, Writing–original draft.

## Funding

The author(s) declare that financial support was received for the research, authorship, and/or publication of this article. This study was supported by the National Natural Science Foundation of China (51874054); National Key R&D Program of China (2023YFC3009001).

## Conflict of interest

The authors declare that the research was conducted in the absence of any commercial or financial relationships that could be construed as a potential conflict of interest.

## Generative AI statement

The author(s) declare that no Generative AI was used in the creation of this manuscript.

## Publisher's note

All claims expressed in this article are solely those of the authors and do not necessarily represent those of their affiliated organizations, or those of the publisher, the editors and the reviewers. Any product that may be evaluated in this article, or claim that may be made by its manufacturer, is not guaranteed or endorsed by the publisher.

## References

- An, M. K., Zhang, F. S., Min, K. B., Elsworth, D., Marone, C., and He, C. R. (2021). The potential for low-grade metamorphism to facilitate fault instability in a geothermal reservoir. *Geophys. Res. Lett.* 48 (11). doi:10.1029/2021gl093552
- Bai, J. Z., Dou, L. M., Li, J. Z., Zhou, K. Y., Cao, J. R., and Kan, J. L. (2022). Mechanism of coal burst triggered by mining-induced fault slip under high-stress conditions: a case study. *Front. Earth Sci.* 10. doi:10.3389/feart.2022.884974
- Ban, L. R., Zhu, C., Hou, Y. H., Du, W. S., Qi, C. Z., and Lu, C. S. (2023). A method to predict the peak shear strength of rock joints based on machine learning. *J. Mt. Sci.* 20 (12), 3718–3731. doi:10.1007/s11629-023-8048-z
- Ben-Zion, Y., and Sammis, C. G. (2003). Characterization of fault zones. *Pure Appl. Geophys.* 160 (3–4), 677–715. doi:10.1007/pl00012554
- Bolton, D. C., Shreedharan, S., McLaskey, G. C., Riviere, J., Shokouhi, P., Trugman, D. T., et al. (2022). The high-frequency signature of slow and fast laboratory earthquakes. *J. Geophys. Research-Solid Earth* 127 (6), e2022JB024170. doi:10.1029/2022jb024170
- Brace, W. F., and Byerlee, J. D. (1966). Stick-slip as a mechanism for earthquakes. *Science* 153 (3739), 990–992. doi:10.1126/science.153.3739.990
- Brantut, N., Passelegue, F. X., Deldicque, D., Rouzaud, J.-N., and Schubnel, A. (2016). Dynamic weakening and amorphization in serpentinite during laboratory earthquakes. *Geology* 44 (8), 607–610. doi:10.1130/g37932.1
- Buijze, L., Guo, Y., Niemeijer, A. R., Ma, S., and Spiers, C. J. (2021). Effects of heterogeneous gouge segments on the slip behavior of experimental faults at dm scale. *Earth Planet. Sci. Lett.* 554, 116652. doi:10.1016/j.epsl.2020.116652
- Cao, S. T., Zhang, F. S., An, M. K., and Yasuhara, H. (2024). Effects of particle size and normal stress on the frictional stability and healing of simulated basalt gouges: implications for lunar seismicity. *Rock Mech. Rock Eng.* 57 (12), 10895–10910. doi:10.1007/s00603-024-04070-7
- Choi, J. H., Edwards, P., Ko, K., and Kim, Y. S. (2016). Definition and classification of fault damage zones: a review and a new methodological approach. *Earth-Science Rev.* 152, 70–87. doi:10.1016/j.earscirev.2015.11.006
- Cvitanovic, N. S., Nikolic, M., and Ibrahimbegovic, A. (2015). Influence of specimen shape deviations on uniaxial compressive strength of limestone and similar rocks. *Int. J. Rock Mech. Min. Sci.* 80, 357–372. doi:10.1016/j.ijrmms.2015.10.008
- Delle Piane, C., Giwelli, A., Ben Clennell, M., Esteban, L., Kiewiet, M., Kiewiet, L., et al. (2016). Frictional and hydraulic behaviour of carbonate fault gouge during fault reactivation - an experimental study. *Tectonophysics* 690, 21–34. doi:10.1016/j.tecto.2016.07.011
- Fagereng, Å., Remitti, F., and Sibson, R. H. J. N. G. (2010). Shear veins observed within anisotropic fabric at high angles to the maximum compressive stress. *Nat. Geosci.* 3 (7), 482–485. doi:10.1038/ngeo898
- Giorgetti, C., Tesei, T., Scuderi, M. G., and Colletini, C. (2019). Experimental insights into fault reactivation in gouge-filled fault zones. *J. Geophys. Research-Solid Earth* 124 (4), 4189–4204. doi:10.1029/2018jb016813
- Guerin-Marthe, S., Kwiatek, G., Wang, L., Bonnelye, A., Martinez-Garzon, P., and Dresen, G. (2023). Preparatory slip in laboratory faults: effects of roughness and load point velocity. *J. Geophys. Research-Solid Earth* 128 (4). doi:10.1029/2022jb025511
- Hou, W. T., Ma, D., Liu, X. W., and Zhang, J. X. (2024). Experimental study on hydraulic and mechanical properties of fault rock under the thermal-hydraulic-mechanical coupling. *Geothermics* 119, 102975. doi:10.1016/j.geothermics.2024.102975
- Jaeger, J. G. M. (1960). Shear failure of anisotropic rocks. *Geol. Mag.* 97 (1), 65–72. doi:10.1017/s0016756800061100
- Ji, Y., Wu, W., and Zhao, Z. (2019). Unloading-induced rock fracture activation and maximum seismic moment prediction. *Eng. Geol.* 262, 105352. doi:10.1016/j.enggeo.2019.105352
- Ji, Y. L., Hofmann, H., Duan, K., and Zang, A. (2022). Laboratory experiments on fault behavior towards better understanding of injection-induced seismicity in geoenery systems. *Earth-Science Rev.* 226, 103916. doi:10.1016/j.earscirev.2021.103916
- Ju, Y., Wan, C. B., Fu, G. M., Ren, Z. Y., Mao, L. T., and Chiang, F. P. (2022). Effects of near-fault stress evolution and surface asperities on rough fault slip: an evaluation based on photoelastic shear tests and additively printed models. *Eng. Geol.* 305, 106715. doi:10.1016/j.enggeo.2022.106715
- Kang, Y. S., Geng, Z., Liu, B., and Huang, Y. Q. (2024). Experimental investigation on fluid-induced slip behavior of fault filled with fault gouge. *J. Rock Mech. Geotechnical Eng.* 16 (9), 3661–3672. doi:10.1016/j.jrmge.2024.02.022
- Ke, C. Y., McLaskey, G. C., and Kammer, D. S. (2018). Rupture termination in laboratory-generated earthquakes. *Geophys. Res. Lett.* 45 (23), 12784–12792. doi:10.1029/2018gl080492
- Leeman, J. R., Saffer, D. M., Scuderi, M. M., and Marone, C. (2016). Laboratory observations of slow earthquakes and the spectrum of tectonic fault slip modes. *Nat. Commun.* 7, 11104. doi:10.1038/ncomms11104
- Li, H. X., Yan, C. G., Shi, Y. L., Lan, H. X., Bao, H., Sun, W. F., et al. (2024a). Failure mechanism and stability evaluation of rockslides with oblique intersecting faults as well as mitigation measures for slope - top platform collapse. *Landslides*. doi:10.1007/s10346-024-02416-4
- Li, Y. T., Fukuyama, E., and Yoshimitsu, N. (2024b). Mining-induced fault failure and coseismic slip based on numerical investigation. *Bull. Eng. Geol. Environ.* 83 (10), 386. doi:10.1007/s10064-024-03888-3
- Liu, H., Si, H., Xu, D. Y., and Long, K. (2024). Laboratory investigation on slip behaviors of fault induced by cyclic confining pressure. *Eng. Geol.* 337, 107575. doi:10.1016/j.enggeo.2024.107575
- Long, K., Zhang, Z. Y., Li, S. H., Li, K., and Luo, Y. (2022). The roles of crack development and water in stress rotation and fault weakening. *Tectonophysics* 823, 229190. doi:10.1016/j.tecto.2021.229190
- Mei, C., Mercuri, M., and Rudnicki, J. W. (2024). Rock friction experiments and modeling under hydrothermal conditions. *Earth-Science Rev.* 254, 104824. doi:10.1016/j.earscirev.2024.104824
- Meng, F. Z., Yue, Z. F., Li, M. Z., Han, J. H., Cai, Q. J., Wang, W., et al. (2023). Frictional sliding behaviour of rough fracture in granite under true triaxial loading with implications for fault reactivation. *Rock Mech. Rock Eng.* 57, 197–217. doi:10.1007/s00603-023-03561-3
- Nilsen, B. (2021). Challenges and some recommendations related to estimation of *in-situ* swelling pressure of gouge materials. *Rock Mech. Rock Eng.* 54 (9), 5141–5147. doi:10.1007/s00603-021-02551-7
- Niu, L. L., Zhu, W. C., Liu, X. G., Wang, J., Liu, K., and Chen, T. Y. (2024). Shear creep deformation of rock fracture distributed by dynamic loading. *Int. J. Rock Mech. Min. Sci.* 183, 105943. doi:10.1016/j.ijrmms.2024.105943
- Pan, W. H., Li, Y. P., Zhang, C., Shi, X. S., Cui, H., Wang, B., et al. (2023). Coal burst prevention technology and engineering practice in ordos deep mining area of China. *Sustainability* 15 (1), 159. doi:10.3390/su15010159
- Rasouli, V., Pallikathakathil, Z. J., and Mawuli, E. (2011). The influence of perturbed stresses near faults on drilling strategy: a case study in Blacktip field, North Australia. *J. Petroleum Sci. Eng.* 76 (1–2), 37–50. doi:10.1016/j.petrol.2010.12.003
- Ren, D. (2024). Friction stabilities of gypsum and kaolinite/calcite mixture fault gouges under high pressure. *Front. Earth Sci.* 11, 1346880. doi:10.3389/feart.2023.1346880
- Ruggieri, R., Scuderi, M. M., Trippetta, F., Tinti, E., Brignoli, M., Mantica, S., et al. (2021). The role of shale content and pore-water saturation on frictional properties of simulated carbonate faults. *Tectonophysics* 807, 228811. doi:10.1016/j.tecto.2021.228811
- Sibson, R. H. (1985). A note on fault reactivation. *J. Struct. Geol.* 7 (6), 751–754. doi:10.1016/0191-8141(85)90150-6
- Su, H. J., Jing, H. W., Zhao, H. H., Yu, L. Y., and Wang, Y. C. (2017). Strength degradation and anchoring behavior of rock mass in the fault fracture zone. *Environ. Earth Sci.* 76 (4), 179. doi:10.1007/s12665-017-6501-4
- Tse, R., and Cruden, D. M. (1979). Estimating Joint Roughness Coefficients. *Int. J. Rock Mech. Min. Sci.* 16 (5), 303–307. doi:10.1016/0148-9062(79)90241-9
- Wang, H., Li, H. B., Si, J. L., Sun, Z. M., and Huang, Y. (2014). Internal structure of the Wenchuan earthquake fault zone, revealed by surface outcrop and WFSD-1 drilling core investigation. *Tectonophysics* 619, 101–114. doi:10.1016/j.tecto.2013.08.029
- Wang, L., Kwiatek, G., Renard, F., Guérin-Marthe, S., Rybacki, E., Bohnhoff, M., et al. (2024). Fault roughness controls injection-induced seismicity. *Proc. Natl. Acad. Sci. U. S. A.* 121 (3), e2310039121. doi:10.1073/pnas.2310039121
- Wang, L., Liu, S. M., Cheng, Y. P., Yin, G. Z., Zhang, D. M., and Guo, P. K. (2017). Reservoir reconstruction technologies for coalbed methane recovery in deep and multiple seams. *Int. J. Min. Sci. Technol.* 27 (2), 277–284. doi:10.1016/j.ijmst.2017.01.026
- Wu, J., Liu, L., Deng, Y. F., Zhang, G. P., Zhou, A. N., and Xiao, H. L. (2022). Use of recycled gypsum in the cement-based stabilization of very soft clays and its micro-mechanism. *J. Rock Mech. Geotechnical Eng.* 14 (3), 909–921. doi:10.1016/j.jrmge.2021.10.002
- Wu, W., Zhao, Z. H., and Duan, K. (2017). Unloading-induced instability of a simulated granular fault and implications for excavation-induced seismicity. *Tunn. Undergr. Space Technol.* 63, 154–161. doi:10.1016/j.tust.2017.01.002
- Wu, X. C., Li, Z. G., Yang, X., Sun, C., Wang, W. T., Almeida, R., et al. (2023). Quantifying and modeling curved thrust fault-propagation folds at different scales. *J. Struct. Geol.* 172, 104888. doi:10.1016/j.jsg.2023.104888
- Wynants-Morel, N., De Barros, L., and Cappa, F. (2021). Sensitivity of the seismic moment released during fluid injection to fault hydro-mechanical properties and background stress. *Front. Earth Sci.* 9. doi:10.3389/feart.2021.638723
- Xu, S. Q., Fukuyama, E., Yamashita, F., Kawakata, H., Mizoguchi, K., and Takizawa, S. (2023). Fault strength and rupture process controlled by fault surface topography. *Nat. Geosci.* 16 (1), 94–100. doi:10.1038/s41561-022-01093-z
- Yaghoubi, A., Dusseault, M. B., and Leonenko, Y. (2022). Injection-induced fault slip assessment in montney formation in western Canada. *Sci. Rep.* 12 (1), 11551. doi:10.1038/s41598-022-15363-8

- Yu, B. W., Chen, J. Y., Spiers, C. J., Ma, S. L., Zhang, M., Qi, W. B., et al. (2024). Frictional properties of simulated fault gouges subject to normal stress oscillation and implications for induced seismicity. *J. Geophys. Research-Solid Earth* 129 (9). doi:10.1029/2024jb029521
- Zhang, C. Q., Xu, J., Jin, S. J., Cui, G. J., Guo, Y. H., and Li, L. Y. (2023). Sliding modes of fault activation under constant normal stiffness conditions. *J. Rock Mech. Geotechnical Eng.* 15 (5), 1213–1225. doi:10.1016/j.jrmge.2022.08.005
- Zhang, F. S., An, M. K., Zhang, L. Y., Fang, Y., and Elsworth, D. (2019). The role of mineral composition on the frictional and stability properties of powdered reservoir rocks. *J. Geophys. Research-Solid Earth* 124 (2), 1480–1497. doi:10.1029/2018jb016174
- Zhang, S. C., Song, S. L., Meng, W. H., Li, Y. Y., and Shen, B. T. (2024). Mechanism and experimental investigation of sudden water inrush hazards in surrounding rock due to shear fracture in deep mining operations. *Petroleum Sci. Technol.*, 1–18. doi:10.1080/10916466.2024.2325600
- Zhang, X., and Sanderson, D. J. (2001). Evaluation of instability in fractured rock masses using numerical analysis methods: effects of fracture geometry and loading direction. *J. Geophys. Research-Solid Earth* 106 (B11), 26671–26687. doi:10.1029/2001jb000311
- Zhong, Z., Xu, C. Q., Wang, L., Hu, Y. J., and Zhang, F. S. (2023). Experimental investigation on frictional properties of stressed basalt fractures. *J. Rock Mech. Geotechnical Eng.* 15 (6), 1457–1475. doi:10.1016/j.jrmge.2022.12.020
- Zhu, C., Karakus, M., He, M. C., Meng, Q. X., Shang, J. L., Wang, Y., et al. (2022). Volumetric deformation and damage evolution of Tibet interbedded skarn under multistage constant-amplitude-cyclic loading. *Int. J. Rock Mech. Min. Sci.* 152, 105066. doi:10.1016/j.ijrmms.2022.105066
- Zhu, C., Xing, X. S., He, M. C., Tang, Z. C., Xiong, F., Ye, Z. Y., et al. (2024). Failure behavior and strength model of blocky rock mass with and without rockbolts. *Int. J. Min. Sci. Technol.* 34 (6), 747–762. doi:10.1016/j.ijmst.2024.06.008